Charged States of Sc3N@C68 : An In Situ Spectroelectrochemical Study of the Radical Cation and Radical Anion of a Non-IPR Fullerene

4 AUTHORS, INCLUDING:

Alexey A Popov

Leibniz Institute for Solid State and Materi…

188 PUBLICATIONS **3,410** CITATIONS

SEE PROFILE

Shangfeng Yang

University of Science and Technology of C…

141 PUBLICATIONS **2,844** CITATIONS

SEE PROFILE

Charged States of Sc$_3$N@C$_{68}$: An In Situ Spectroelectrochemical Study of the Radical Cation and Radical Anion of a Non-IPR Fullerene

Peter Rapta,[†,‡] Alexey A. Popov,[†,§] Shangfeng Yang,[†,¥] and Lothar Dunsch*[,†]

Group of Electrochemistry and Conducting Polymers, Leibniz-Institute for Solid State and Materials Research Dresden, D-01171 Dresden, Germany, Department of Physical Chemistry, Faculty of Chemical and Food Technology, Slovak University of Technology, SK-81237 Bratislava, Slovak Republic, and Chemistry Department, Moscow State University, Moscow 119992, Russia

Received: March 27, 2008

The redox behavior of Sc$_3$N@C$_{68}$ is studied systematically by means of electrochemistry, in situ ESR/Vis−NIR spectroelectrochemistry, and detailed theoretical treatment. Formation of the negatively and positively charged paramagnetic species for the same trimetallic nitride endohedral fullerene is demonstrated for the first time. The electrochemical study of Sc$_3$N@C$_{68}$ exhibits two electrochemically irreversible but chemically reversible reduction steps and two reversible oxidation steps. A double-square reaction scheme is proposed to explain the observed redox reaction at cathodic potentials involving the reversible dimerisation of the Sc$_3$N@C$_{68}$ monoanion. The spin state of the radical cation and the radical anion is probed by ESR spectroscopy, indicating that in both states, the large part of the unpaired spin is delocalized on the fullerene cage. The charged states of the non-isolated pentagon rule fullerene are characterized furthermore by in situ absorption spectroscopy. The interpretation of experimental data is supported by the density functional theory (DFT) calculations of the spin distribution in the anion and cation radicals of Sc$_3$N@C$_{68}$ and time-dependent DFT calculations of the absorption spectra of the charged species.

Introduction

Endohedral fullerenes with an encaged trimetallic nitride cluster (clusterfullerenes) have been attracting great interest since their discovery in 1999[1] because of the feasibility of tuning the trapped metal atoms and stabilizing a large variety of cage sizes with different isomeric structures.[2–13] It has been recently discussed how much the variation of the cluster size can be extended[3,14] and how the leading forces for the stabilization of endohedral structures have been revealed.[15] Sc$_3$N@C$_{68}$ discovered in 2000[16] is a unique member of the clusterfullerene family because it was the first clusterfullerenes with the cage violating the isolated pentagon rule (IPR; note, however, that several new non-IPR nitride clusterfullerenes have been discovered recently).[9,10,12,17] The non-IPR carbon cage with D_3 symmetry (isomer 6140) was proven for this clusterfullerene by means of NMR[16] and single-crystal X-ray studies.[18] However, despite the increased interest in such unusual structures, only few spectroscopic and theoretical studies of Sc$_3$N@C$_{68}$ have been reported up to now.[19–22] The electronic structure and vibrational spectra of Sc$_3$N@C$_{68}$ were studied in detail experimentally and with theoretical computations in our group.[22] Although the electronic structure of trimetallic nitride clusterfullerenes is formally conceived as a result of a six-fold electron transfer from the cluster to the carbon cage, it was shown that the effect of Sc$_3$N encapsulation in the C$_{68}$ cage is more complicated, with a significant hybridization of the cluster and the cage orbitals.[20,22]

* To whom correspondence should be addressed. E-mail: L.Dunsch@ifw-dresden.de.
† Leibniz-Institute for Solid State and Materials Research Dresden.
‡ Slovak University of Technology.
§ Moscow State University.
¥ New address: Hefei National Laboratory for Physical Sciences at Microscale & Department of Materials Science and Engineering, University of Science and Technology of China, Hefei 230026, China.

The cluster-to-cage electron transfer in the clusterfullerenes implies that the surplus electron density is localized on the fullerene and hence raises the question of the redox behavior of these molecules. Systematic electrochemical studies of clusterfullerenes including Sc$_3$N@C$_{80}$ (I),[6,23,24] Tm$_3$N@C$_{80}$ (I),[25] Dy$_3$N@C$_{2n}$ ($2n$ = 78, 80),[26] Y$_3$N@C$_{80}$,[27] Er$_3$N@C$_{80}$,[27] Gd$_3$N@C$_{2n}$ ($2n$ = 80, 84, 88),[28] and Sc$_3$N@C$_{78}$[24] were reported in the past few years by our group[6,25,26] and by the others.[23,24,27,28] A strong dependence of the electrochemical redox behavior and frontier molecular orbitals (highest occupied molecular orbital (HOMO) and lowest unoccupied molecular orbital (LUMO)) on the cage size and the structure and a significant contribution of the cluster to both the LUMO and the HOMO were found.

By decreasing the fullerene cage size to C$_{68}$ and by encapsulating the trimetallic nitride cluster in such a small cage, a substantial change in the LUMO and the HOMO is expected as compared to larger cage sizes. Thus, the detailed analysis of different Sc$_3$N@C$_{68}$ redox states appears an interesting point to be studied. Recently, we reported the electrochemically generated stable radical cation of Sc$_3$N@C$_{68}$ as confirmed by in situ ESR/Vis−NIR spectroelectrochemistry.[29] The spin state of such radical cation was probed, indicating that the large part of the unpaired spin is delocalized over the fullerene cage. The anodic redox behavior of Sc$_3$N@C$_{68}$ is quite different from that in the cathodic range, where a more complex redox behavior was found. The complex redox behavior in the cathodic part, with strongly shifted reoxidation peaks both for the anion and dianion, appears to be typical for nonfunctionalized M$_3$N@C$_{2n}$ endohedral fullerenes,[6,23,25–28] and the observation of the corresponding paramagnetic anions of M$_3$N@C$_{2n}$ endohedral fullerenes is up to now limited only to the [Sc$_3$N@C$_{80}$]$^{•−}$[30] and [Y$_3$N@C$_{80}$C$_4$H$_9$N]$^{•−}$.[31] In this work, we performed a detailed spectroelectrochemical and theoretical study on the charge transfer at Sc$_3$N@C$_{68}$ with the focus on the formation of both

the corresponding anion and cation radicals. To interpret the observed complex redox behavior in the cathodic part, a reaction scheme is proposed, including the reversible chemical reaction of the $Sc_3N@C_{68}$ monoanion induced by the charging of the cage. DFT calculations of the optimal geometry parameters, charge, and spin density distribution of the neutral and charged forms of $Sc_3N@C_{68}$ are performed to reveal the influence of the electrochemical reduction/oxidation on the molecular structure of the clusterfullerene, and time-dependent DFT calculations are used to explain the absorption spectra of the electrochemically generated species.

Experimental Details

The synthesis of $Sc_3N@C_{68}$ was reported previously.[22] Chemical identification and purity of the studied $Sc_3N@C_{68}$ clusterfullerene was established by the laser desorption time-of-flight (LD-TOF) mass spectrometry and by high performance liquid chromatography (HPLC) analysis.

For a typical electrochemical and spectroelectrochemical study, the $Sc_3N@C_{68}$ sample dissolved in toluene was dried and transferred as a powder into a glove box (oxygen and water content below 1 ppm), where it was immediately redissolved in 1,2-dichlorobenzene (o-DCB, anhydrous, 99%, Aldrich) at concentrations ranging from 1×10^{-4} to 5×10^{-4} mol L^{-1}. Tetrabutylammonium tetrafluoroborate or hexaflourophosphate (TBABF$_4$ or TBAPF$_6$, Fluka, dried under reduced pressure at 340 K for 24 h prior to use) was added as the supporting electrolyte at concentrations of 0.1–0.2 mol L^{-1}. The cyclic voltammograms and the square-wave voltammograms were obtained with a PAR 273 potentiostat (EG&G, Gaithersburg, MD) in a three-electrode system with platinum wires as working and counter electrodes and a silver wire as pseudo-reference electrode under glove-box conditions. For fast scan voltammetry, a platinum microelectrode was used. Ferrocene (Fc) was added as the internal standard after each voltammetric measurement series, and all potentials are given versus the Fc/Fc$^+$ couple. A PG 284 potentiostat (HEKA, Germany) was used for the potential control in the in situ ESR/UV–Vis–NIR spectroelectrochemical studies. ESR spectra were recorded by the EMX X-Band ESR spectrometer (Bruker, Germany), and optical spectra were obtained simultaneously by the UV–Vis–NIR spectrometer system TIDAS (J&M, Aalen, Germany).

Computational Details

Geometry optimization and time-dependent DFT calculations of $Sc_3N@C_{68}$ and its charged states were performed by using PBE functional[32] and PRIRODA quantum-chemical code.[33,34] The code employed expansion of the electron density in an auxiliary basis set to accelerate evaluation of the Coulomb and exchange-correlation terms.[33] A TZ2P-quality basis set with SBK[35] effective core potential for Sc atoms as implemented in PRIRODA was used for optimization; no symmetry constraints were adopted. TD-DFT calculations were performed with a reduced basis set of double-zeta quality (DZ hereafter). Testing calculations have shown that the use of such a moderate basis set for the neutral $Sc_3N@C_{68}$ did not result in qualitative changes in the predicted excitation spectra as compared to the results of calculations with TZ2P basis set reported earlier.[22] Point-energy calculations at the B3LYP/6-311G* level of theory were performed with the use of PC GAMESS.[36] DFTB[37] calculations were performed with the use of deMon software.[38]

Results and Discussion

Cyclic Voltammetry of $Sc_3N@C_{68}$. Figure 1 shows a cyclic voltammogram of $Sc_3N@C_{68}$ in o-DCB/TBABF$_4$ solutions

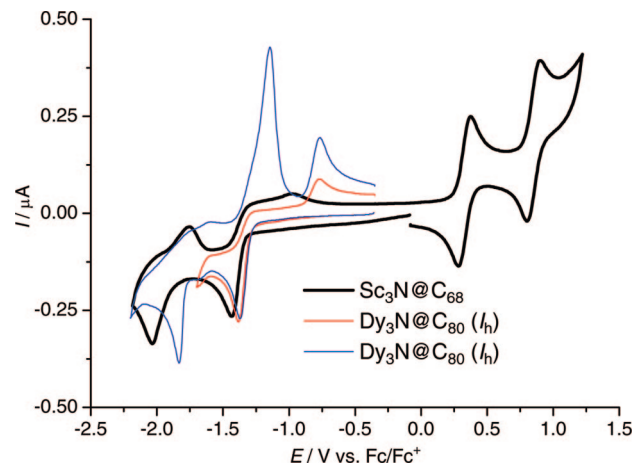**Figure 1.** Cyclic voltammetry of the non-IPR D_3 $Sc_3N@C_{68}$ (black) and the I_h $Dy_3N@C_{80}$ (red and blue lines) in 0.1 M TBAPF$_6$-o-DCB solution at a scan rate of 0.1 V s^{-1}.

performed at both the cathodic and the anodic potentials and compared to the voltammetric data of $Dy_3N@C_{80}$. The cyclic voltammogram of $Sc_3N@C_{68}$ exhibits two electrochemically irreversible but chemically reversible reduction steps similar to the reduction of other $M_3N@C_{2n}$ clusterfullerenes.[6,25–28] The first reduction step of $Sc_3N@C_{68}$ at a scan rate of 0.1 V s^{-1} clearly indicates the first reduction peak and the strongly shifted reoxidation peak of those species formed by the fullerene monoanion. The electrochemical energy gap of $Sc_3N@C_{68}$ of 1.71 V, which is obtained as the difference between the redox potential of the first oxidation step and the redox potential of the first reduction step, is considerably smaller than that of $Sc_3N@C_{80}$ (I_h), being 1.86 V.[6] This is consistent with the results obtained for their optical energy gaps determined previously by UV–Vis–NIR spectroscopy and DFT computations.[22]

No significant change in the shape and intensity of the reduction peaks during the multiple redox cycles for $Sc_3N@C_{68}$ was observed. A further confirmation of the chemical reversibility of the redox reactions was obtained by LD-TOF mass-spectroscopy measurements performed with the sample solutions after the voltammetric measurements and also exhausting electrolysis. They reveal that the peaks of the corresponding clusterfullerene dominated the mass spectra in all cases, and no stable follow-up products of the clusterfullerenes were detected. Because the electrochemical reduction is chemically reversible and no reaction with the solvent was observed by mass spectrometry after multiple cycling, the follow-up processes can be attributed either to intramolecular structural changes in the anion or to a reaction between the reduced species.

Spectroelectrochemistry of $Sc_3N@C_{68}$. To get a deeper insight into the possible electrode processes during the first reduction step of $Sc_3N@C_{68}$, we performed an exhaustive electrolysis in the ESR cavity at potentials of the first reduction step and detected an ESR signal which could be attributed to the anion radical of $Sc_3N@C_{68}$ (Figure 2a). Similar to the $[Sc_3N@C_{68}]^{\bullet+}$ radical cation (Figure 2b), the characteristic ESR pattern of the anion includes 22 lines with the intensity distribution characteristic for three equivalent Sc nuclei. However, the hyperfine splitting of the Sc atoms in the anion is slightly increased to 1.75 G as compared to 1.28 G found for the cation radical. Additionally, the g value of the anion, 2.0023, is substantially larger than the g value of the cation, 2.0010. If the ESR spectrum of $[Sc_3N@C_{68}]^{\bullet-}$ is compared to the spectrum of $[Sc_3N@C_{80}]^{\bullet-}$ anion radical, which also exhibits 22 lines, a
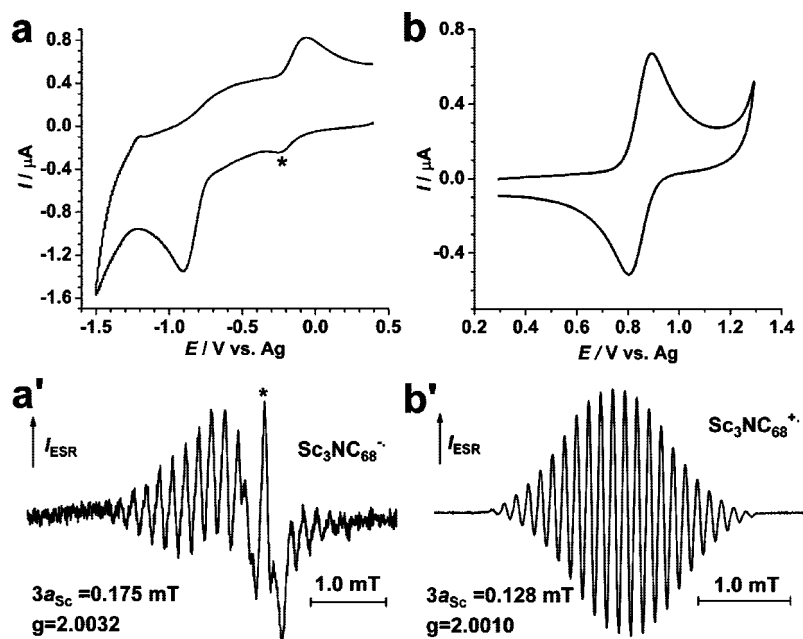
Figure 2. In situ cyclic voltammograms ($V = 3$ mV s^{-1}) and representative ESR spectra of (a) [Sc$_3$N@C$_{68}$]$^{•-}$ and (b) [Sc$_3$N@C$_{68}$]$^{•+}$ radical ions observed in situ in the course of reduction and oxidation in 0.1 M TBAPF$_6$/o-DCB at the first oxidation peak and at the first reduction peak, respectively (asterisk denotes a narrow impurity signal at g ∼2.0005).
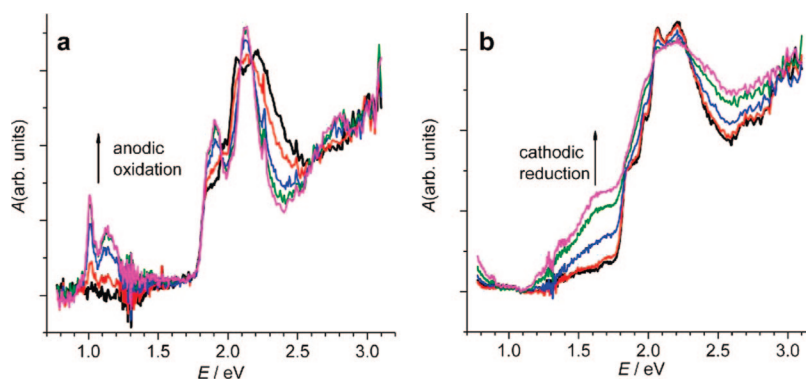

Figure 3. Absorption spectra of Sc$_3$N@C$_{68}$ in 0.1M TBAPF$_6$-o-DCB solution at room temperature under spectroelectrochemical conditions in the potential range of (a) the first oxidation and (b) the first reduction peak.

significant difference occurs. The latter exhibits a Sc hyperfine splitting of 55.6 G and a g factor of 1.9984, both pointing to the localization of the spin density of the [Sc$_3$N@C$_{80}$]$^{•-}$ on the cluster. In contrast, the comparably small Sc hyperfine spitting constants found for the anion and cation radicals of Sc$_3$N@C$_{68}$ indicate that the cluster has a minor contribution to the spin density and to the frontier orbitals.

Importantly, the concentration of the [Sc$_3$N@C$_{68}$]$^{•-}$ detected by ESR spectroscopy was much smaller than the concentration of the radical cation [Sc$_3$N@C$_{68}$]$^{•+}$ generated with the same sample under the same experimental conditions, which confirms the low stability of Sc$_3$N@C$_{68}$ radical anion. This fact leads to the conclusion that the major part of Sc$_3$N@C$_{68}$ monoanion forms diamagnetic species at the first reduction step.

Because the Vis−NIR spectra of the charged fullerenes used in the characterization of the corresponding anions and cations provide important information on their electronic structure, we also performed in situ ESR/Vis−NIR spectroelectrochemical studies on Sc$_3$N@C$_{68}$, both in the anodic and in the cathodic potential range where the ion radicals are generated. As shown in our recent communication,[29] the generation of the stable radical monocation [Sc$_3$N@C$_{68}$]$^{•+}$ was clearly identified upon oxidation of Sc$_3$N@C$_{68}$ by in situ ESR/Vis−NIR spectroelec-

trochemistry. New NIR absorption bands with maxima at 1.13 eV (1100 nm) and 1.01 eV (1226 nm) are observed for the cation (Figure 3a), whereas the absorption spectrum in the visible range is more similar to the spectrum of the neutral form and exhibits two intense bands at 1.91 eV (651 nm) and 2.13 eV (583 nm). As shown in Figure 3, there is a substantial difference in the electronic spectra of positively and negatively charged Sc$_3$N@C$_{68}$ (Figure 3b). In contrast to the cationic form, the species formed in the reduction of Sc$_3$N@C$_{68}$ do not exhibit detectable NIR features down to 0.8 eV, the range accessible with our spectrometer. In the visible range, the bands are much broader than those in the pristine Sc$_3$N@C$_{68}$, and a new, poorly resolved band is developed at around 1.62 eV (770 nm).

DFT Calculations. To rationalize the observed ESR and Vis−NIR spectra of the charged Sc$_3$N@C$_{68}$ states, we have performed DFT calculations of the structure, spin density distribution, and excitation spectra of the monoanion and monocation of Sc$_3$N@C$_{68}$. First, the geometry of the charged species was optimized at the PBE/TZ2P level. The calculations have shown that the charging of Sc$_3$N@C$_{68}$ does not result in dramatic changes of the geometry parameters of the cage and the cluster (Table 1, Figure 4). As the HOMO and the LUMO of Sc$_3$N@C$_{68}$ have both A_1 symmetry,[22] the ground electronic

TABLE 1: DFT-Optimized Bond Lengths (in Angstroms), Natural Charges (q), and Hyperfine Splitting Constants (a, in Gauss) in Sc$_3$N@C$_{68}$, [Sc$_3$N@C$_{68}$]$^{\bullet+}$ and [Sc$_3$N@C$_{68}$]$^{\bullet-a}$

	Sc$_3$N@C$_{68}$	cation	Δ^c	anion	Δ^c
		C−C Bond Distances^b			
a	1.445	1.448	0.003	1.447	0.002
b	1.455	1.454	−0.001	1.460	0.004
c	1.470	1.465	−0.004	1.465	−0.005
d	1.451	1.457	**0.006**	1.452	0.001
e	1.446	1.441	**−0.006**	1.445	−0.001
f	1.454	1.446	**−0.008**	1.454	0.000
g	1.462	1.477	**0.015**	1.459	−0.003
h	1.437	1.432	−0.005	1.444	**0.007**
i	1.436	1.435	−0.001	1.430	**−0.006**
j	1.416	1.416	0.000	1.423	**0.006**
k	1.449	1.448	−0.001	1.454	0.005
l	1.443	1.443	0.000	1.441	−0.001
m	1.445	1.445	0.000	1.453	**0.008**
n	1.429	1.429	−0.001	1.426	−0.004
o	1.450	1.451	0.002	1.458	**0.008**
p	1.440	1.438	−0.001	1.440	0.001
q	1.440	1.439	−0.001	1.441	0.001
r	1.432	1.431	−0.001	1.432	0.000
Sc−N	1.993	1.988	−0.005	1.999	0.005
Sc−C	2.313	2.314	0.001	2.304	−0.009
		Natural Charge			
q(Sc)	1.433	1.422	−0.010	1.444	0.012
q(N)	−1.575	−1.569	0.006	−1.586	−0.011
		Hyperfine Splitting Constants			
a(Sc)		−1.376		−2.536	
a(N)		0.050		0.112	

^{a} Bond lengths are optimized at the PBE/TZ2P level, whereas natural charges and hyperfine splitting constants are calculated at the B3LYP/6-311G*//PBE/TZ2P level. ^{b} See Figure 4 for the bond labeling system used in this work. ^{c} Difference from the corresponding values in the neutral state; the largest changes of the bondlengths are highlighted in bold.

states of both the cation and the anion have the $^2A_1$ symmetry, and hence, the addition or removal of one electron to/from Sc$_3$N@C$_{68}$ does not result in changes of the molecular symmetry. In the cation, the Sc−N bonds become slightly shorter, whereas in the anion, they are slightly longer compared to the neutrally charged Sc$_3$N@C$_{68}$. The largest changes of C−C bondlengths in the cation do not exceed 0.008 Å.
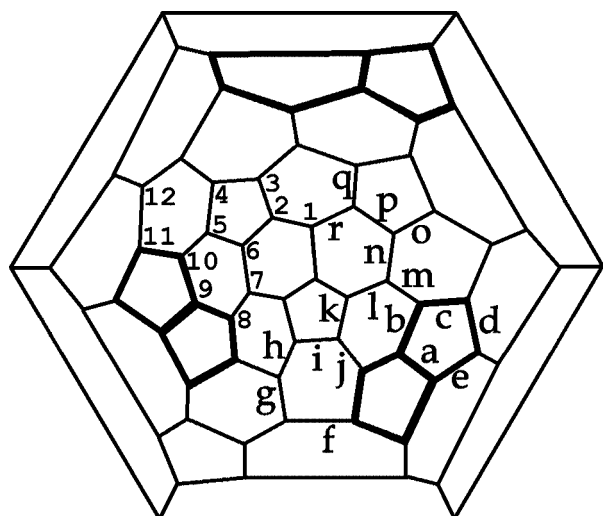
Figure 4. Schlegel diagram of C$_{68}$ and labeling of the atoms (1−12) and C−C bonds (**a**−**g**) adopted in this work. Adjacent pentagons are shown in bold.
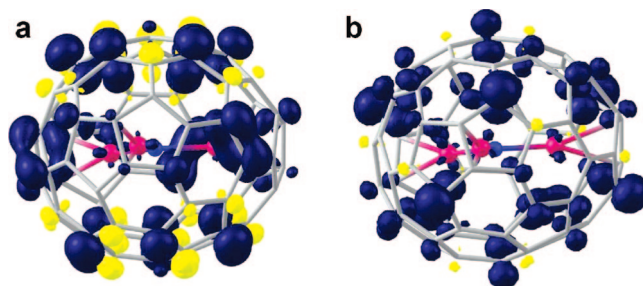
Figure 5. Spin density distribution in [Sc$_3$N@C$_{68}$]$^{\bullet+}$ (left) and [Sc$_3$N@C$_{68}$]$^{\bullet-}$ (right) as computed at the B3LYP/6-311G*//PBE/TZ2P level of theory.

monoanion, the bond **g** (Figure 4) is elongated by 0.015 Å, whereas the changes in all other parameters do not exceed 0.007 Å (Table 1).

The point-energy calculations with the B3LYP/6-311G* method were performed to reveal the spin density distribution and the hyperfine constants (Table 1). The B3LYP-computed a(Sc) hyperfine constant for the cation is −1.38 G in perfect agreement with the experimental value of 1.28 G (Figure 2). For the anion, the calculations predict a(Sc) = −2.54 G. This value is somewhat larger than the experimentally observed $|a$(Sc)$|$ = 1.75 G, but the overall qualitative agreement of the computed and experimental data is also apparent. In agreement with the comparably small a(Sc) values in both charged species, the calculations predict that the major part of the spin density in the anion and the cation is localized on the carbon cage with very modest contribution on the Sc atoms (Figure 5). Because the spin density distribution on the carbon cage is substantially different in the cation and the anion, the differences in the a(Sc) values of these species are to be explained in this manner (Figure 5). In particular, the spin density in the cation is largely localized near the bonds of type **g** and the atoms of C3 and C6 type, close to the poles of the cage, whereas the largest spin density in the anion is found for the atoms of C8 type located in the adjacent pentagons (see Figure 4 for the labeling of the atoms in Sc$_3$N@C$_{68}$). The analysis of the natural charges of the Sc and N atoms in the different states of Sc$_3$N@C$_{68}$ (Table 1) shows that the charging of the clusterfullerene results in very minor changes of the cluster charge state, which is in line with the delocalization of the spin density over the carbon cage.

To interpret the changes in the Vis−NIR absorption spectra observed during reduction and oxidation of Sc$_3$N@C$_{68}$, we have performed TD-DFT calculations of the excitation spectra of the cation and anion (Tables 2 and 3). Figure 6 shows MO levels of the neutral Sc$_3$N@C$_{68}$ as well as the schematic presentation of orbital occupancies in the cationic state and the most intense transitions which can be assigned to the experimental spectra, and Figure 7 compares the experimental and calculated excitation spectra for the neutral Sc$_3$N@C$_{68}$ and its charged forms. The spectrum predicted for the cation shows a perfect agreement with the experimental data. Namely, the most intense transitions in the NIR range are expected because of the two excitations: HOMO − 2 → SOMO ($1^2A_1 \rightarrow 1^2A_2$, E = 1.01 eV) and HOMO − 3 → SOMO ($1^2A_1 \rightarrow 2^2E$, E = 1.13 eV). These transitions perfectly correspond to the experimentally observed bands at 1.01 and 1.13 eV, respectively (marked as I and II in Figure 7b). Note that the SOMO → LUMO excitation in [Sc$_3$N@C$_{68}$]$^{\bullet+}$ is optically forbidden (because it yields an excited state of A_1 symmetry, and only transitions to A_2 and E symmetric states are allowed), whereas the HOMO − 1 → SOMO ($1^2A_1 \rightarrow 1^2E$, E = 0.49 eV) excitation, although formally allowed, is expected

TABLE 2: Most Intense[a] Low Energy Excitations in the Sc₃N@C₆₈ Cation: Experimental Data and TD-DFT Calculations

ex. state	exp. E, eV	calc. E, eV	f	leading configurations (%)[b]
1^2A_2	1.01	1.013	0.00632	HOMO − 2 → SOMO (98)
2^2E	1.13	1.129	0.00755	HOMO − 3 → SOMO (99)
3^2A_2		1.671	0.00103	HOMO − 6 → SOMO (97)
5^2E	1.86[c]	1.840	0.00607	SOMO → LUMO + 2 (54), HOMO − 1 → LUMO (39)
6^2E		1.893	0.00555	HOMO − 7 → SOMO (52), SOMO → LUMO + 2 (24), HOMO − 1 → LUMO (20)
7^2E	1.91	1.961	0.03024	HOMO − 7 → SOMO (45), HOMO − 1 → LUMO (24), SOMO → LUMO + 2 (18)
9^2E		2.128	0.00387	HOMO − 1 → LUMO + 1 (87)
10^2E	2.13	2.154	0.03546	SOMO → LUMO + 4 (76)
7^2A_2		2.286	0.00160	HOMO − 1 → LUMO + 2 (59), HOMO − 2 → LUMO (38)
12^2E		2.313	0.00355	HOMO − 1 → LUMO + 2 (66), HOMO − 3 → LUMO (30)

[a] Only excitations with $f > 0.001$ are listed; the full list of excitations in this energy range can be found in the Supporting Information. [b] Contributions less than 10% are omitted. [c] Shoulder at the peak at 1.91 eV.

TABLE 3: Most Intense[a] Low Energy Excitations in the Sc₃N@C₆₈ Anion: TD-DFT Calculations

ex. state	calc. E, eV	f	leading configurations (%)[b]
1^2A_2	0.498	0.00180	SOMO → LUMO + 1 (100)
1^2E	0.654	0.00153	SOMO → LUMO + 2 (99)
2^2E	0.884	0.00267	SOMO → LUMO + 4 (99)
3^2E	1.322	0.00240	SOMO → LUMO + 5 (99)
2^2A_2	1.357	0.00270	SOMO → LUMO + 6 (99)
5^2E	1.745	0.00721	HOMO − 1→SOMO (77), SOMO → LUMO + 9 (14)
4^2A_2	1.782	0.00153	HOMO → LUMO + 1 (100)
6^2E	1.801	0.00760	SOMO → LUMO + 9 (84), HOMO − 1 → SOMO (12)
8^2E	1.969	0.01200	HOMO → LUMO + 2 (82)
12^2E	2.125	0.00156	SOMO → LUMO + 13 (66), HOMO − 1 → LUMO + 1 (19), HOMO → LUMO + 4 (13)

[a] Only excitations with $f > 0.001$ are listed; the full list of excitations in this energy range can be found in the Supporting Information. [b] Contributions less than 10% are omitted.

to have a very low intensity. Besides, this transition is beyond the range accessible by our spectrometer. At higher energy, the excitation spectrum of [Sc₃N@C₆₈]•⁺ resembles that of the neutral molecule, with a slight shift of the energies and changes in the oscillator strengths. Experimental absorption bands at 1.91 and 2.13 eV (marked as III and IV in Figure 6b) are assigned to the calculated excitations $1^2A_1 → 7^2E$ ($E = 1.96$ eV) and $1^2A_1 → 10^2E$ ($E = 2.15$ eV). The latter is analogous to the excitation in the neutral Sc₃N@C₆₈ and can be described presumably by a SOMO → LUMO + 4 excitation, whereas the former is more complex in nature (see Table 2).

TD-DFT calculations predict a more complex excitation pattern for the anion (Table 3). Because the density distribution of the unoccupied MOs in Sc₃N@C₆₈ is very high in the anion, it gives rise to the multiple SOMO → LUMO + N excitation with a relatively low energy (Figures 6 and 7). Note that the intensities of the NIR transitions in the anion are considerably lower than those in the cation. The agreement with the experimental spectrum is worse as compared to that of the cation, indicating that the spectrum observed for the anion corresponds to a mixture of the anion radical and its diamagnetic follow-up product which is already discussed in the cyclovoltammetric studies above. Thus, the worse correspondence between the computed and experimental spectra of the anion should be understood by taking into account that the reduction is electrochemically irreversible and the major part of the reduction product is ESR silent. Therefore, the absorption

spectrum observed experimentally should also include the contribution from the species other than the fullerene monoanion, and because the major part seems to be ESR silent, this contribution should be dominant. Therefore, it is not surprising that the calculated absorption spectrum of the anion shows a poor agreement with the experimental spectrum.

Redox Mechanism at Cathodic Potentials. Because the reduction of Sc₃N@C₆₈ is chemically reversible and the reaction with the solvent can be ruled out, the follow-up processes at the first reduction step can be attributed either to the intramolecular structural changes in the anion or to the reaction between the reduced species. However, the intramolecular rearrangement is not consistent with the formation of EPR silent species. To fully rule out this possibility, we have tried to find other possible positions of the cluster inside the cage in the Sc₃N@C₆₈ monoanion by the use of DFT computations, but the optimization always resulted in the configuration described above (Table 1), which is only marginally different from the uncharged state.

Therefore, we propose that the formation of the diamagnetic species at the first reduction step may be the result of the
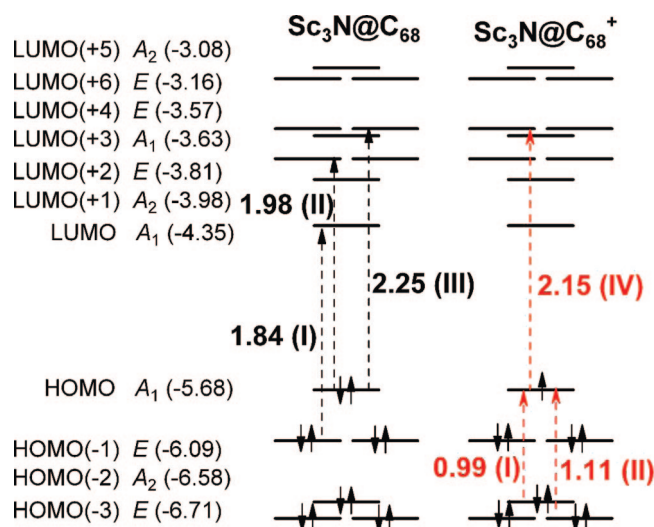

Figure 6. MO levels of the neutral Sc₃N@C₆₈ (left) with their symmetries and energies as computed at the PBE/DZ level, and schematic representation of MO occupancies in the [Sc₃N@C₆₈]•⁺ (right). The most intense transitions are shown by the black (neutral state) and red (cation) arrows. The number at each arrow is the excitation energy predicted by TD-DFT (in eV), and roman numbers correspond to the bands marked in the experimental spectra (Figure 7). Note that the excitation corresponding to band III in the spectrum of [Sc₃N@C₆₈]•⁺ cannot be described by a single configuration (see Table 2) and hence is not marked on the figure.
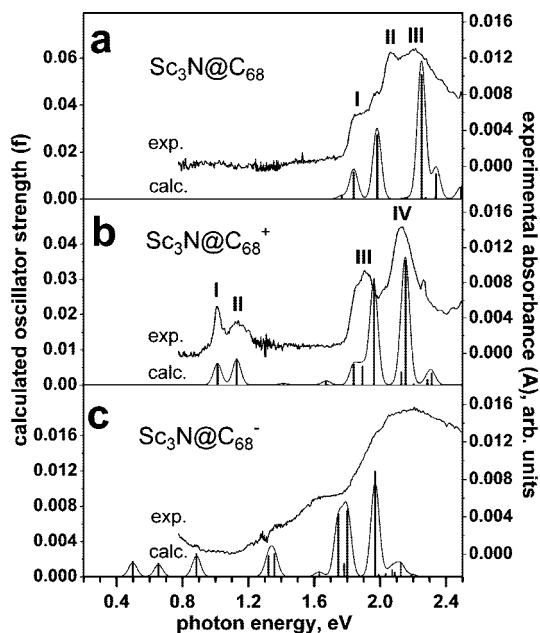
Spectroelectrochemical Study of Non-IPR Clusterfullerene Sc$_3$N@C$_{68}$

J. Phys. Chem. A, Vol. 112, No. 26, 2008 **5863**

Figure 7. Experimental spectra of the neutral Sc$_3$N@C$_{68}$ (a), its cation (b), and the product of cathodic reduction (c) compared to the results of TD-DFT calculations of the excitation spectra for neutral and positively and negatively charged Sc$_3$N@C$_{68}$. Roman numbers in the experimental spectra of Sc$_3$N@C$_{68}$ and [Sc$_3$N@C$_{68}$]$^{•+}$ mark the most intense bands, the assignment of which is provided in Figure 6.

SCHEME 1: Double-Square Reaction Scheme of the Electrochemical Redox Reaction of Sc$_3$N@C$_{68}$[a]
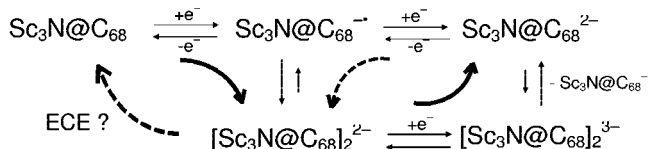
[a] The stable species generated by the structural rearrangement or other follow-up reaction are marked by asterisks. The arc arrows show the main reaction pathways.

reversible dimerization of the anion. The dimer is then decomposed into the monomeric species at the second reduction because of the higher charge at the cage or (in the reversed scan) at the reoxidation potential at less cathodic values than expected for a reversible reaction of the monoanion to form the neutral monomer. This complex redox behavior is explained in detail by the double-square reaction scheme given for the Sc$_3$N@C$_{68}$ reduction (Scheme 1). As shown in Figure 1, the shift of the reoxidation peak in the range of the second electron transfer is much lower than that of Dy$_3$N@C$_{80}$(I$_h$), indicating a redox behavior of Sc$_3$N@C$_{68}$ different than that of Dy$_3$N@C$_{80}$(I$_h$), for which an internal rearrangement of cluster was proposed.[26] In the region of the first reduction peak of Sc$_3$N@C$_{68}$, one electron is transferred to the initially neutral Sc$_3$N@C$_{68}$(0), generating its monoanion Sc$_3$N@C$_{68}$(−1). This reduction step is followed by a dimerisation reaction resulting in the formation of the dimer dianion (Sc$_3$N@C$_{68}$)$_2$$^{2-}$ (see DFT-optimized molecular structure of the (Sc$_3$N@C$_{68}$)$_2$$^{2-}$ dimer in Figure 9, which will be discussed later). The reoxidation of the dimer dianion (Sc$_3$N@C$_{68}$)$_2$$^{2-}$ occurs at more positive potentials than expected for a reversible reoxidation of the monoanion generating the initial Sc$_3$N@C$_{68}$(0). A large potential peak-to-peak separation is therefore observed at conventional scan rates, although the redox reaction is chemically reversible under the given conditions. Consequently, in contrast to the Sc$_3$N@C$_{68}$
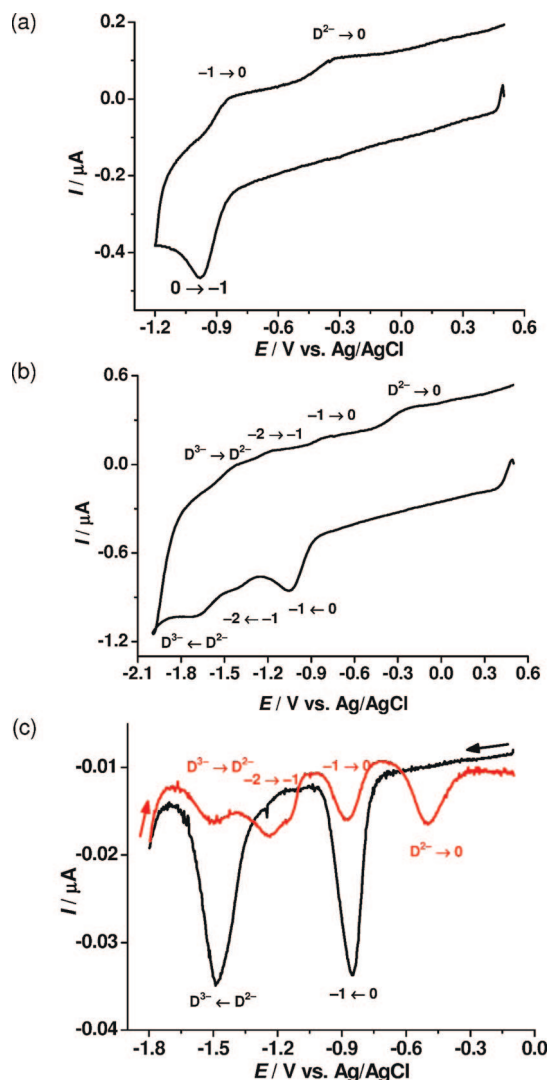

Figure 8. Fast-scan cyclic voltammetry at (a) 25 V s^{-1} and (b) 75 V s^{-1} and (c) square-wave voltammetry (75 mV s^{-1}; step height, 3 mV; pulse amplitude, 50mV; pulse duration, 0.02 s; black line, forward scan; red line, back scan) of Sc$_3$N@C$_{68}$ in 0.2 M TBABF$_4$/o-DCB solution (Ag/AgCl wire, reference electrode; Pt, working electrode).

oxidation,[29] the anion radical of Sc$_3$N@C$_{68}$ is less stable. Obviously, an equilibrium of the monoanion with its dimeric form exists, as summarized in the reaction scheme in Scheme 1.

To support the reaction scheme of the Sc$_3$N@C$_{68}$ reduction (Scheme 1) and to confirm the formation of dimeric dianion which cannot be identified by other spectroscopic techniques (e.g., NMR or mass spectrometry) because of its limited stability, we performed fast-scan cyclic voltammetry as well as square-wave voltammetry of the Sc$_3$N@C$_{68}$ reduction. The results of both techniques are given in Figure 8. In contrast to the low scan-rate case (Figure 1), the pattern of the cyclic voltammogram for Sc$_3$N@C$_{68}$ reduction substantially changes at high scan rates, and new voltammetric peaks arise by increasing the scan rate (Figure 8a,b). To understand the observed voltammetric behavior of Sc$_3$N@C$_{68}$, fast-scan cyclic voltammetry with scan rates up to 75 V s^{-1} was done, and the square-wave voltammetric technique was applied both in the forward scan and in the back scan (Figure 8c). The larger potential peak−peak separations in the cyclic voltammograms at higher scan rates can be understood by the uncompensated internal resistance drop in the electrochemical cell. In the first reduction step

(step 0 → −1 in Figure 8a), one electron is transferred to the neutral $Sc_3N@C_{68}$ (0), and its monoanion $[Sc_3N@C_{68}]^{\bullet-}$ is generated (see Scheme 1), as was unambiguously confirmed by in situ ESR spectroelectrochemistry described above.

This reduction step is followed by a fast (relative to the timescale of the voltammetric experiment) reversible dimerisation, resulting in the formation of dimeric dianion $[Sc_3N@C_{68}]_2^{2-}$ (marked as D^{2-} in Figure 8). The reoxidation of the dimer D^{2-} to the neutral initial $Sc_3N@C_{68}$ occurs at more positive potentials than expected for the reversible reoxidation of the monoanion. Such a reoxidation peak is denotedas $D^{2-} → 0$ in Figure 8a,b. At high scan rates, a new anodic peak (step −1 → 0 in Figure 8a) attributed to the reoxidation of monoanion $[Sc_3N@C_{68}]^{\bullet-}$ to the neutral $Sc_3N@C_{68}$ is already observable at the potential expected for the reversible voltammetric behavior. Both these reoxidation processes including the step −1 → 0 as well as the reoxidation of dimer ($D^{2-} → 0$) are completely observable in Figure 8c in the back scan in the square-wave voltammetric experiment (performed in the glove box in the same solution of $Sc_3N@C_{68}$ and in the same voltammetric cell as the other voltammetric experiments). Upon reduction at more negative potentials at high scan rates, we observed exclusively a direct reduction of the unstable monoanion to dianion and its reoxidation (steps −1 → −2 and −2 → −1 in Figure 8b). As already shown in Scheme 1, the reduction of dimeric dianion is expected to be a complex process because of the decomposition of the dimer into the dianion and the monoanion. The destruction of the reduced dimer occurs because of the strong Coulomb repulsion in the higher charged state. This process is seen in Figure 8c in the range of the second electron transfer. The second square-wave voltammetric peak in the forward scan is much broader than the first reduction peak, indicating more complex processes than the simple reduction of dimeric dianion to dimer trianion. In the back scan, a very small peak corresponding to the reoxidation of dimer trianion was observed, confirming the low stability of triply charged dimer. Additionally, two new reoxidation peaks are observable at lower potentials in the back scan. One of them corresponds to the reoxidation of monomer dianion to the monoanion, as already confirmed by fast-scan voltammetry. The monoanion is not stable and dimerises again. The small shoulder observed in the back scan at about −1.1 V versus Ag/AgCl, the relative intensity of which is dependent on the scan rate, is tentatively attributed to the redox processes accompanied by the dimer formation. Very recent electrochemical studies of trimetallonitride endohedral fullerenes indicate the influence of the solvent on the reduction behaviour,[24] as well as the strong influence of the derivatisation (termination of reactive sites on the cage) of trimetallonitride endohedrals to the reversibility of reduction processes,[27] supporting our reaction scheme which includes a reversible dimerisation. It is well known that the reversible dimerisation, very often observed and described in detail in the field of short organic π-conjugated oligomers, strongly depends on the solvent as well as on the presence of reactive sites on the oligomer chain.[39]

To explore the possibility of a reversible dimerisation of $[Sc_3N@C_{68}]^{\bullet-}$, we have performed theoretical studies of the dimerization of the $Sc_3N@C_{68}$ anion. As C_{68} has 12 symmetry-non-equivalent atoms (Figure 4), it gives rise to the 66 inter-cage bonding motifs, each being presented by several structural and rotational conformers. Calculations for selected dimerization motifs have shown that the energy differences between the conformers were in the order of 1−2 kJ/mol, and thus, only one structure of each type was considered at the first stage.
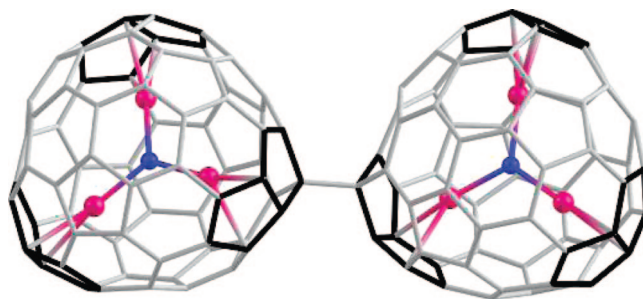

Figure 9. DFT-optimized molecular structure of the C8−C8′ $(Sc_3N@C_{68})_2^{2-}$ dimer (C_2 symmetry).

Because of the high computational requirements, the computations were first performed at the DFTB level, and then, the DFT calculations were performed for the lowest-energy structures. In agreement with the common chemical intuition, both DFTB and DFT favor the formation of the dimer linked through C8 atoms, which have the highest contribution to the spin density (Figure 9).

Stable structures were also obtained by linking the fullerene cages through C8−C10′ (7 kJ/mol above C8−C8′ isomer, prime means that the atom is in a different cage) or C10−C10′ atoms (16 kJ/mol above C8−C8′ isomer). The lowest energy dimer structures have also the highest HOMO−LUMO gap, which is equal to 1.0 eV for C8−C8′ structure and 0.1−0.15 eV smaller for other dimeric structures. Thus, in contrast to the monomeric radical anion, a dimer should not exhibit strong absorptions in the NIR range. Because such NIR absorptions are not found experimentally, this interpretation could explain the disagreement between the computed (for the monomeric form) and the experimental spectra. Therefore, it supports the conclusion drawn from the spectroelectrochemical as well as the voltammetric studies.

Conclusions

In this work, we have performed a detailed electrochemical, spectroelectrochemical, and theoretical study of the redox behavior of the non-IPR clusterfullerene $Sc_3N@C_{68}$. The formation of negatively and positively charged states of a paramagnetic trimetallic nitride endohedral fullerene is demonstrated for the first time by applying in situ ESR/Vis−NIR spectroelectrochemistry. The spin density distribution in $[Sc_3N@C_{68}]^{\bullet+}$ and $[Sc_3N@C_{68}]^{\bullet-}$ was computed at the B3LYP/6-311G*//PBE/TZ2P level. Both the experimental and the theoretical results confirm that in both charged states (cation and anion), the larger part of the unpaired spin is delocalized on the fullerene cage. To interpret the changes in the Vis−NIR absorption spectra observed during the electrochemical reduction and oxidation of $Sc_3N@C_{68}$, TD-DFT calculations of the excitation spectra of the cation and anion were performed. A double-square reaction scheme was proposed to explain the observed redox behavior of the monoanion involving its reversible dimerisation. The results of the fast-scan cyclovoltammetry and of the square-wave voltammetry of $Sc_3N@C_{68}$ support our interpretation of the reaction scheme for $Sc_3N@C_{68}$ reduction.

Supporting Information Available: Tables of the full list of TD-DFT predicted excitation energies of Sc$_3$N@C$_{68}$ anion and cation in the visible range. This material is available free of charge via the Internet at http://pubs.acs.org.

References and Notes

(1) Stevenson, S.; Rice, G.; Glass, T.; Harich, K.; Cromer, F.; Jordan, M.R.; Craft, J.; Hadju, E.; Bible, R.; Olmstead, M.M.; Maitra, K.; Fisher, A.J.; Balch, A.L.; Dorn, H.C. *Nature* **1999**, *401* (6748), 55–57.

(2) For a recent review see Dunsch, L.; Yang, S. *Small* **2007**, *3* (8), 1298–1320.

(3) Dunsch, L.; Yang, S. F. *Phys. Chem. Chem. Phys.* **2007**, *9* (24), 3067–3081.

(4) Dunsch, L.; Bartl, A.; Georgi, P.; Kuran, P. *Synth. Met.* **2001**, *121* (1−3), 1113–1114.

(5) Dunsch, L.; Krause, M.; Noack, J.; Georgi, P. *J. Phys. Chem. Solids* **2004**, *65* (2−3), 309–315.

(6) Krause, M.; Dunsch, L. *ChemPhysChem* **2004**, *5* (9), 1445–1449.

(7) Krause, M.; Wong, J.; Dunsch, L. *Chem.-Eur. J.* **2005**, *11* (2), 706–711.

(8) Yang, S. F.; Dunsch, L. *J. Phys. Chem. B* **2005**, *109* (25), 12320–12328.

(9) Yang, S. F.; Popov, A. A.; Dunsch, L. *Angew. Chem., Int. Ed.* **2007**, *46* (8), 1256–1259.

(10) Yang, S.; Popov, A. A.; Dunsch, L. *J. Phys. Chem. B* **2007**, *111* (49), 13659–13663.

(11) Olmstead, M. H.; de Bettencourt-Dias, A.; Duchamp, J. C.; Stevenson, S.; Marciu, D.; Dorn, H. C.; Balch, A. L. *Angew. Chem., Int. Ed.* **2001**, *40* (7), 1223–1225.

(12) Beavers, C. M.; Zuo, T. M.; Duchamp, J. C.; Harich, K.; Dorn, H. C.; Olmstead, M. M.; Balch, A. L. *J. Am. Chem. Soc.* **2006**, *128* (35), 11352–11353.

(13) Zuo, T.M.; Beavers, C. M.; Duchamp, J. C.; Campbell, A.; Dorn, H. C.; Olmstead, M. M.; Balch, A. L. *J. Am. Chem. Soc* **2007**, *129* (7), 2035–2043.

(14) Yang, S. F.; Dunsch, L. *Angew. Chem., Int. Ed.* **2006**, *45* (8), 1299–1302.

(15) Popov, A. A.; Dunsch, L. *J. Am. Chem. Soc.* **2007**, *129* (38), 11835–11849.

(16) Stevenson, S.; Fowler, P. W.; Heine, T.; Duchamp, J. C.; Rice, G.; Glass, T.; Harich, K.; Hajdu, E.; Bible, R.; Dorn, H. C. *Nature* **2000**, *408* (6811), 427–428.

(17) Popov, A. A.; Krause, M.; Yang, S. F.; Wong, J.; Dunsch, L. *J. Phys. Chem. B* **2007**, *111* (13), 3363–3369.

(18) Olmstead, M. M.; Lee, H. M.; Duchamp, J. C.; Stevenson, S.; Marciu, D.; Dorn, H. C.; Balch, A. L. *Angew. Chem., Int. Ed.* **2003**, *42* (8), 900–903.

(19) Park, S. S.; Liu, D.; Hagelberg, F. *J. Phys. Chem. A* **2005**, *109* (39), 8865–8873.

(20) Liu, D.; Hagelberg, F.; Park, S. S. *Chem. Phys.* **2006**, *330* (3), 380–386.

(21) Reveles, J. U.; Heine, T.; Koster, A. M. *J. Phys. Chem. A* **2005**, *109* (32), 7068–7072.

(22) Yang, S. F.; Kalbac, M.; Popov, A.; Dunsch, L. *Chem., Eur. J.* **2006**, *12* (30), 7856–7863.

(23) Elliott, B.; Yu, L.; Echegoyen, L. *J. Am. Chem. Soc.* **2005**, *127* (31), 10885–10888.

(24) Zhang, L.; Chen, N.; Fan, L.; Wang, C.; Yang, S. *J. Electroanal. Chem.* **2007**, *608*, 15–21.

(25) Krause, M.; Liu, X. J.; Wong, J.; Pichler, T.; Knupfer, M.; Dunsch, L. *J. Phys. Chem. A* **2005**, *109* (32), 7088–7093.

(26) Yang, S. F.; Zalibera, M.; Rapta, P.; Dunsch, L. *Chem.-Eur. J.* **2006**, *12* (30), 7848–7855.

(27) Cardona, C. M.; Elliott, B.; Echegoyen, L. *J. Am. Chem. Soc.* **2006**, *128* (19), 6480–6485.

(28) Chaur, M. N.; Melin, F.; Elliott, B.; Athans, A. J.; Walker, K.; Holloway, B. C.; Echegoyen, L. *J. Am. Chem. Soc.* **2007**, *129* (47), 14826–14829.

(29) Yang, S. F.; Rapta, P.; Dunsch, L. *Chem. Commun.* **2007**, (2), 189–191.

(30) Jakes, P.; Dinse, K. P. *J. Am. Chem. Soc.* **2001**, *123* (36), 8854–8855.

(31) Echegoyen, L.; Chancellor, C. J.; Cardona, C. M.; Elliott, B.; Rivera, J.; Olmstead, M. M.; Balch, A. L. *Chem. Commun.* **2006**, (25), 2653–2655.

(32) Perdew, J. P.; Burke, K.; Ernzerhof, M. *Phys. Rev. Lett.* **1996**, *77* (18), 3865–3868.

(33) Laikov, D. N. *Chem. Phys. Lett.* **1997**, *281*, 151–156.

(34) Laikov, D. N.; Ustynuk, Y. A. *Russ. Chem. Bull.* **2005**, *54* (3), 820–826.

(35) Stevens, W. J.; Krauss, M.; Basch, H.; Jasien, P. G. *Can. J. Chem.* **1992**, *70*, 612–630.

(36) Granovsky, A. A. *PC GAMESS*, version 7.0; 2007. http://classic-.chem.msu.su/gran/gamess/index.html.

(37) Porezag, D.; Frauenheim, T.; Köhler, T.; Seifert, G.; Kaschner, R. *Phys. Rev. B* **1995**, *51*, 12947–12960.

(38) Köster, A. M.; Calaminici, P.; Casida, M. E.; Flores-Moreno, R.; Geudtner, G.; Gourost, A.; Heine, T.; Ipatov, A.; Janetzko, F.; del Campo, J. M.; Patchkovskii, S.; Reveles, J. U.; Salahub, D. R.; Vela, A. http://www.deMon-software.com, 2006.

(39) Rapta, P.; Schulte, N.; Schluter, A. D.; Dunsch, L. *Chem.-Eur. J.* **2006**, *12* (11), 3103–3113, and references therein.